Tailoring topological nature of merging bound states in the continuum by manipulating structure symmetry of the all-dielectric metasurface

Guangcheng Sun ⬤, Yue Wang ⬤,* Yaohe Li ⬤, Zijian Cui ⬤, and Wenshuo Chen ⬤

Key Laboratory of Ultrafast Photoelectric Technology and Terahertz Science in Shaanxi, Xi'an University of Technology, Xi'an 710054, China

Kuang Zhang ⬤

Department of Microwave Engineering, Harbin Institute of Technology, Harbin 150001, China

Photonic bound states in the continuum (BIC) promise a versatile platform for construction of optical resonators with highly confined electromagnetic fields and ultralong radiative lifetime. Merging multiple BIC can enable suppression of out-of-plane radiative losses and further boost the quality (Q) factor of the resonance state. However, current studies on merging BIC (M-BIC) are primarily restricted to the elementary BIC with topological charge ±1, which hinders further improvement of the performance of optical resonators. Here, an all-silicon terahertz metasurface (THz-MS) is investigated that supports the symmetry-protected BIC (SP-BIC) with topological charge -2 and accidental BIC (A-BIC) with topological charge ±1 simultaneously. Empowered by the topological nature of BIC, we merge twelve A-BIC with a higher-order SP-BIC at the Γ point. By tailoring in-plane mirror symmetry of the THz-MS, we achieve M-BIC at almost arbitrary position in the momentum space. Unlike original isolated BIC, M-BIC manifests the dramatic enhancement of the Q factors of nearby resonances and are robust against radiation losses introduced by fabrication imperfections. Our work presents a paradigm for realizing higher-order at-Γ M-BIC and momentum-steerable M-BIC that can substantially enhance light-matter interaction and further improve the performance of terahertz optoelectronic devices.

DOI: 10.1103/PhysRevB.109.035406

I. INTRODUCTION

The ability to confine and localize light is of particular importance for miscellaneous photonic applications that require strong light-matter interaction, such as lasers [1,2], higher-harmonic generation [3–5], and nonlinear and quantum effects [6–9]. Conventional light-trapping schemes, including total internal reflection, photonic band gap, and highly disordered media, rely on materials or systems that forbid outgoing waves to achieve light localization [10,11]. One particularly promising approach to trap light is to exploit the so-called bound states in the continuum (BIC) [12,13]. Photonic BIC refers to a special class of nonradiative electromagnetic eigenstates with infinite lifetime and zero resonance linewidth, even though their frequencies lie inside the continuous leaky radiation spectrum above the light cone and below the diffraction limit [14–16]. All-dielectric metasurfaces (MS) have emerged as a powerful photonic platform for the experimental investigation of BIC due to their high refractive index and intrinsic low dissipation loss [9,11,12,17]. BIC-driven MS holds considerable application potential in ultrasensitive biochemical sensing [18,19], enhanced lasing [20,21], vortex beams [22,23], and nonlinear enhancement [24,25].

BIC are demonstrated as vortex singularities (*V* point) in polarization directions of far-field radiation defined in the *k* space which carry conserved and quantized topological charges [14,26,27]. The generation, evolution, and annihilation of BIC was predicted by their unique topological features [26]. Nevertheless, in practical photonic systems, BIC inevitably appear as quasi-BIC (supercavity mode) with a superhigh but decaying quality (Q) factor due to material absorption, fabrication imperfections, structure disorders, and finite-size effects [28]. Exploiting the topological features of BIC, multiple BIC on the same photonic band can be tuned to a chosen *k* point to form a merging BIC (M-BIC), for example, accidental BIC (A-BIC or off-Γ BIC) merge with a symmetry-protected BIC (SP-BIC) at the Γ point or with a Friedrich-Wintgen BIC at the off-Γ point [1,25,28–30]. M-BIC can suppress the out-of-plane scattering losses and thus enhance the Q factors of nearby resonance compared with original isolated BIC. To date, most of the reported M-BIC are primarily limited to the elementary BIC with topological charges ±1 [1,25,28,29]. Higher-order BIC have topological charge greater than 1 and are excited on higher energy bands or in the system with high-symmetry point groups. From the perspective of topological charge conservation, higher-order BIC can be considered as the collection of several elementary BIC, and thereby it is naturally predicted that merging higher-order BIC undoubtedly further enhances the robustness of the merging state against the ineluctable manufacturing imperfections. In addition, higher-order at-Γ BIC can be split into two off-Γ BIC by reducing the symmetry of the system from C_{6v} to C_{2v} point groups [31], which makes it possible to form M-BIC at an off-Γ point on the isolated lower band. Off-Γ M-BIC have enabled an array of applications requiring

*wangyue2017@xaut.edu.cn

035406-1

angular (wave-vector) tunability, such as on-chip beam steering [32], directional vector beams [33,34], angle-multiplexed ultrasensitive sensors [35,36], and diffraction-free beams [37].

Herein, we employ the topological physics of BIC for constructing M-BIC with higher-order topological charge in an all-dielectric THz-MS and realize M-BIC at an arbitrary k point in the momentum space. To be more specific, we consider the THz-MS composed of silicon (Si) as the photonic platform because of its low loss characteristics in the spectral region of interest. We analyze the C_{6v} characteristics of the proposed THz-MS and reveal that it can excite the SP-BIC with topological charge −2 at the Γ point and several A-BIC with topological charge ±1 at the accidental in-plane wave vector. Under the variation of structural parameters, the higher-order SP-BIC is fixed at the Γ point, while A-BIC moves toward the Γ point due to their sensitivity to the structural parameters and then merge with the higher-order SP-BIC at the Γ point. When break C_{6v} symmetry but preserve C_{2v} symmetry, the initially higher-order SP-BIC splits into two off-Γ BIC with topological charges of −1. By tuning the THz-MS thickness, these two split BIC (S-BIC) remerge with each other at the Γ point or merge with A-BIC at the off-Γ point. Under different combinations of thickness and rotation angle, the broken all in-plane inversion symmetries enable M-BIC to appear at an arbitrary position in the momentum space.

II. RESULTS AND DISCUSSION

A. Merging higher-order BIC at the Γ point

We begin with considering a THz-MS composed of a honeycomb array of circular air holes patterned in a freestanding Si membrane with lattice constant $a = 200\,\mu m$, hole diameter $D = 100\,\mu m$, and thickness $t = 210\,\mu m$, as shown in Fig. 1(a). The refractive index of Si was set as 3.45 in the THz frequency region. All the eigenmodes supported by the THz-MS can be categorized as transverse electric (TE-like) and transverse magnetic (TM-like) modes; here we focus only on TE-like modes. The eigenmode analysis was performed by using the finite-element method provided by commercial software COMSOL MULTIPHYSICS. A numerically simulated TE-like band structure above the light cone along the M-Γ-K direction is shown in Fig. 1(b), and the lowest band (referred to as the TE$_1$ band) we focus on hereafter is marked with a red line. The calculated normalized radiation loss along the highly symmetric M-Γ-K direction is shown in Fig. 1(c), where the TE$_1$ band exhibits a BIC state at the origin (Γ point) and A-BIC at the accidental wave vector ($k_{BIC} = \pm 0.272\pi/a$) away from the Γ point. The inset shows a mode profile of the z component of the magnetic field, H_z, highlighting that the eigenmode on the TE$_1$ band at the Γ point belongs to the B_1 irreducible representation of the C_{6v} point group and hence excites an at-Γ SP- BIC with topological charge $q = -2 + 6n$ [26,31]. The calculated scattering powers of electromagnetic multipole decomposition inside the unit cell (see Fig. S2 of the Supplemental Material [38]) demonstrates that the SP-BIC is dominated by the in-plane electric quadrupole, which results from forbidden coupling due to symmetry mismatch between the eigenmode and the incident plane wave. For A-BIC, the dominant in-plane electric quadrupole interferes destructively
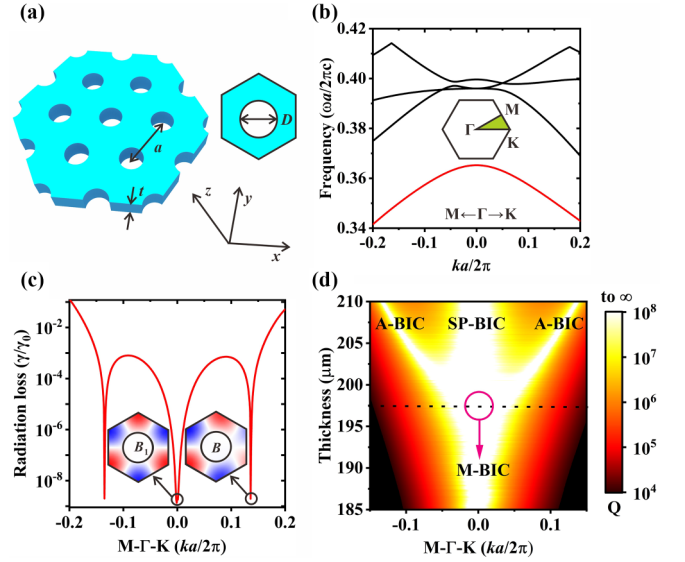

FIG. 1. (a) Left panel: Schematic view of a conventional THz-MS with a hexagonallattice of etched circular holes standing in free space. Right panel: Top view of the hexagonal-lattice unit cell. (b) Numerically simulated TE-like band structure. The inset shows the first Brillouin zone of the triangular lattice and irreducible contour for circular-hole THz-MS (shaded triangle area). (c) Calculated radiation loss (γ) normalized by the value near the light cone (γ_0), γ/γ_0, along both M-Γ and Γ-K direction as a function of $k(a/2\pi)$. The inset shows mode profile of the z component of the magnetic field H_z, highlighting B_1 irreducible representation for the SP-BIC and B irreducible representation for the A-BIC on the TE$_1$ band, respectively. (d) Simulated 2D brightness map of evolution of radiative Q factor for the TE$_1$ band along the M-Γ-K direction wave vector with the variation of the THz-MS thickness.

with weak in-plane electric dipole, in-plane magnetic dipole, in-plane toroidal dipole and in-plane magnetic quadrupole in the far field. These multipole decomposition results agree well with the fundamental nature of the lowest TE-like mode of the MS with C_{6v} photonic lattice [1,26].

To reveal the topological nature of the BIC state, we can project the two-dimensional (2D) polarization vector of far-field radiation in the sp plane, $\mathbf{c}(\mathbf{k}) = c_x(\mathbf{k})\hat{x} + c_y(\mathbf{k})\hat{y}$, onto structure plane ($xy$ plane) and map it into the momentum space ($k_x k_y$ plane). Topological charge q carried by the BIC state for polarization vector $\mathbf{c}(\mathbf{k})$ is defined as the number of times that the polarization vector winds around the vortex [26,39,40]:

$$q = \frac{1}{2\pi} \oint_L d\mathbf{k} \cdot \nabla_{\mathbf{k}} \phi(\mathbf{k}). \tag{1}$$

Here L is a closed loop around the polarization singularity in the k space, traversed in the counterclockwise direction. $\phi(k) = \frac{1}{2}\arg[S_1(\mathbf{k}) + iS_2(\mathbf{k})]$ denotes the angle that the long axis of the polarization ellipse makes with the x axis, where S_i represents the Stokes parameters of $\mathbf{c}(\mathbf{k})$, with $S_0 = |c_x|^2 + |c_y|^2$, $S_1 = |c_x|^2 - |c_y|^2$, $S_2 = 2\text{Re}(c_x^* c_y)$, $S_3 = -2\text{Im}(c_x c_y^*)$. Topological charge q must be an integer if a closed trajectory L encloses a V point where $S_1 = S_2 = S_3 = 0$ [31,41]. Because the magnitude of S_3 is extreme small
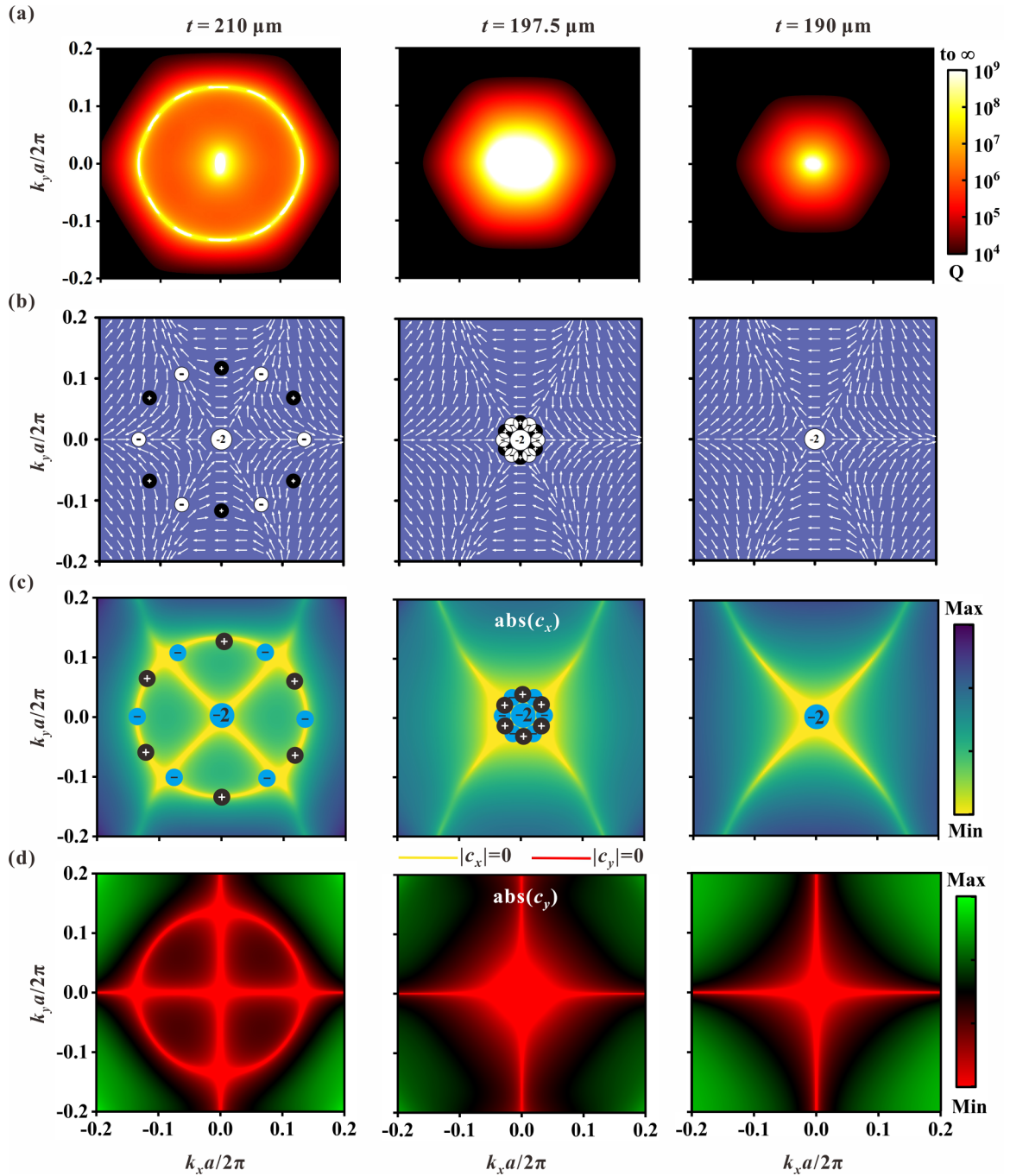
FIG. 2. Numerically calculated Q factors (a), polarization vectors of far-field radiation (b), and the distribution of absolute value of the nodal lines of c_x (c) and c_y (d) near the V point in the momentum space at $t = 210\,\mu m$ (before merging), $t = 197.5\,\mu m$ (at merging), and $t = 190\,\mu m$ (after merging). When the slab thickness is reduced from 210 to 190 μm, twelve A-BIC with topological charge ± 1 at distance $|k_{BIC}| = 0.272\pi/a$ from the origin are gradually merge into an isolated SP-BIC with topological charge -2.

in the wave-vector range of interest (see Fig. S3 of the Supplemental Material [38]), the polarization vector is almost linear and thus the polarization angle becomes $\phi(\mathbf{k}) = \arg[c_x(\mathbf{k}) + ic_y(\mathbf{k})]$ [30]. The calculated radiative Q factor and polarization vector of far-field radiation for the TE$_1$ band at $t = 210\,\mu m$ are plotted in Figs. 2(a) and 2(b), left panel. The diverging Q factor indicates that the TE$_1$ band has a SP-BIC and a ring-shaped envelope of A-BIC in momentum space.

The polarization vector winds twice around the Γ point and once around the k_{BIC} point, respectively. A resonance turns into a BIC when the outgoing power is zero, which happens if and only if $c_x = c_y = 0$ [26]. Therefore the true BIC states correspond to the intersections between nodal lines of $c_x = 0$ and $c_y = 0$ in the k space. We also calculate the 2D color map of nodal lines of c_x and c_y for $t = 210\,\mu m$ shown in Figs. 2(c) and 2(d), left panel, and find nodal lines of $c_x = 0$ and $c_y = 0$
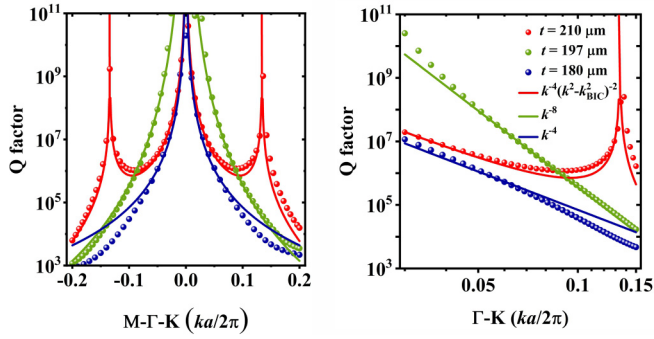
FIG. 3. Simulated radiative Q factors (dotted lines) and the corresponding fitting curves (solid lines) at $t = 210 \, \mu m$ (before merging), 197.5 μm (at merging), and 190 μm (after merging). The Q factors of M-BIC configuration (blue) are orders of magnitude higher than the other isolated BIC design (red and dark green) along both the Γ-M and Γ-K directions due to the scaling rule changes to $Q \propto 1/k^8$.

are singly degenerate at $k_{BIC} = \pm 0.272\pi/a$ and doubly degenerate at the Γ point. These results manifest that a SP-BIC with charge $q = -2$ excites at the Γ point, and six A-BIC with charge $q = +1$ located on the Γ-M direction and six A-BIC with charge $q = -1$ reside at the Γ-K high-symmetry lines. To visually observe the merging process of BIC, we also plot the 2D brightness map of the Q factor for the TE$_1$ band as a function of THz-MS thickness t along the highly symmetric M-Γ-K direction, as shown in Fig. 1(d). As the thickness decreases from 210 μm, the twelve A-BIC gradually move towards the Γ point from the M-Γ and K-Γ directions, respectively, while SP-BIC is always fixed at the Γ point. The SP-BIC and A-BIC collide at $t = 197.5 \, \mu m$, which corresponds to the M-BIC configuration, as illustrated in Fig. 2, middle panel. When t further decreases to 190 μm, A-BIC with opposite topological charges annihilate each other, leaving only a SP-BIC with charge $q = -2$, as shown in Fig. 2, right panel.

The geometrical decay of Q factors in the momentum space can be theoretically derived from the expansions of a Taylor series of c_x and c_y according to $Q \propto 1/|\phi(\mathbf{k})|^2$ [28]. Therefore, for isolated BIC with a topological charge $q = \pm n$, the scaling rule of the Q factor follows $Q \propto 1/k^{2n}$. Obviously, the decay rate of the Q factors in the vicinity of isolated BIC states can be significantly reduced by selecting BIC with higher-order topological charge. Furthermore, when multiple off-Γ BIC with $q = \pm 1$ exist at high-symmetry direction in the k space and have equal distances k_{BIC} from the isolated SP-BIC, the scaling rule is modified to $Q \propto 1/[k^n(k^2 - k_{BIC}^2)]^2$. In the limit $k_{BIC} \to 0$, namely, the special case of topological transition, the scaling rule of M-BIC asymptotically turns to $Q \propto 1/k^{2n+4}$. Therefore, compared with the case of isolated BIC, the merging of the SP-BIC and A-BIC with topological charge $q = \pm 1$ can theoretically increase the Q factor by four orders of magnitude. Further detailed discussion on the scaling rule of the Q factor can be found in Sec. S1 of the Supplemental Material [38]. We calculate the Q-factor distribution of the TE$_1$ band at different thicknesses to verify the scaling rules in different topological configurations, as shown in Fig. 3, where the Q factor in a merging-BIC design (green) is tremendously enhanced over those in an isolated
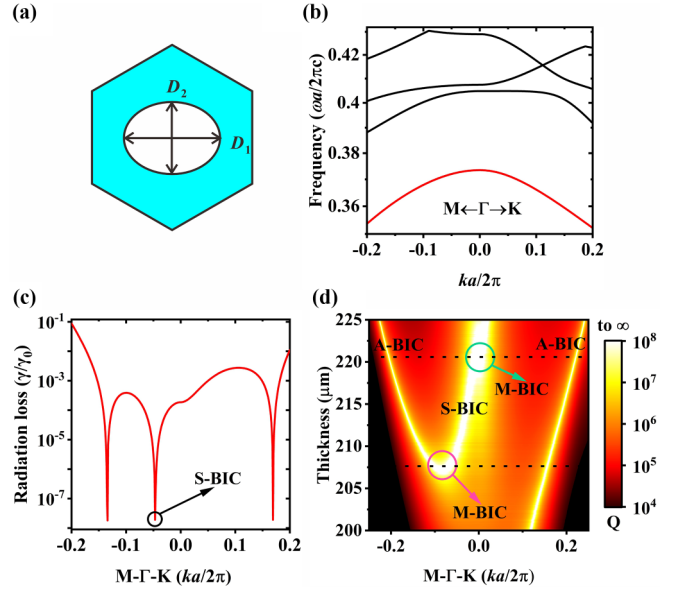

FIG. 4. (a) Schematic drawing of the unit cell with elliptic air holes. The semimajor axis of the ellipse $D_1 = 120 \, \mu m$ and the semiminor axis $D_2 = 100 \, \mu m$. (b) Numerically simulated dispersion relation for a symmetry-reduced THz-MS at $t = 210 \, \mu m$. (c) Calculated radiation loss (γ) normalized by the value near the light cone (γ_0), γ/γ_0, along the highly symmetrical M-Γ-K direction as a function of $k(a/2\pi)$. Owing to the reduced symmetry of the system, the SP-BIC at the Γ point splits into two off-Γ BIC in the Γ-M direction. (d) The evolution trajectory of BIC in momentum space with variation of the slab thickness.

BIC design (red and blue). When the SP-BIC and A-BIC coexist at $t = 210 \, \mu m$, the Q factor geometrically decays as $Q \propto 1/[k^2(k^2 - k_{BIC}^2)]^2$ away from the Γ point. A topological transition occurs as the charges merge at $t > 197.5 \, \mu m$, and A-BIC annihilate and only the SP-BIC is preserved. The $Q \propto 1/k^4$ scaling rule in the vicinity of the Γ point is restored after merging and being kept with the decreasing thickness even to $t = 190 \, \mu m$. In contrast, for the M-BIC configuration at $t = 197.5 \, \mu m$, $k_{BIC} \to 0$ and the scaling rule become $Q \propto 1/k^8$. Previous work has theoretically and experimentally demonstrated M-BIC in a photonic crystal slab with a square lattice of cylindrical air holes, where the SP-BIC possesses a charge $q = +1$, thus improving scaling rule of Q value from $1/k^2$ to $1/k^6$ [28]. Here we further enhance the scaling rule of the Q factor to $1/k^8$, which verifies the distinct advantage of higher-order at-Γ SP-BIC compared with fundamental at-Γ SP-BIC in constructing M-BIC.

B. Merging BIC at the off-Γ point in momentum space

Next we introduce a scenario where the cylindrical air holes are replaced by elliptic cylindrical air holes with the semimajor axis along the x axis while keeping the other structural parameters of the THz-MS unchanged, as represented schematically in Fig. 4(a). This perturbation breaks the C_{6v} symmetry of the system but preserves the C_{2v} symmetry. The TE$_1$ band structure of the elliptic-hole THz-MS is similar to that of the circular-hole THz-MS, except for some minor distortions that result from the reduction of the system
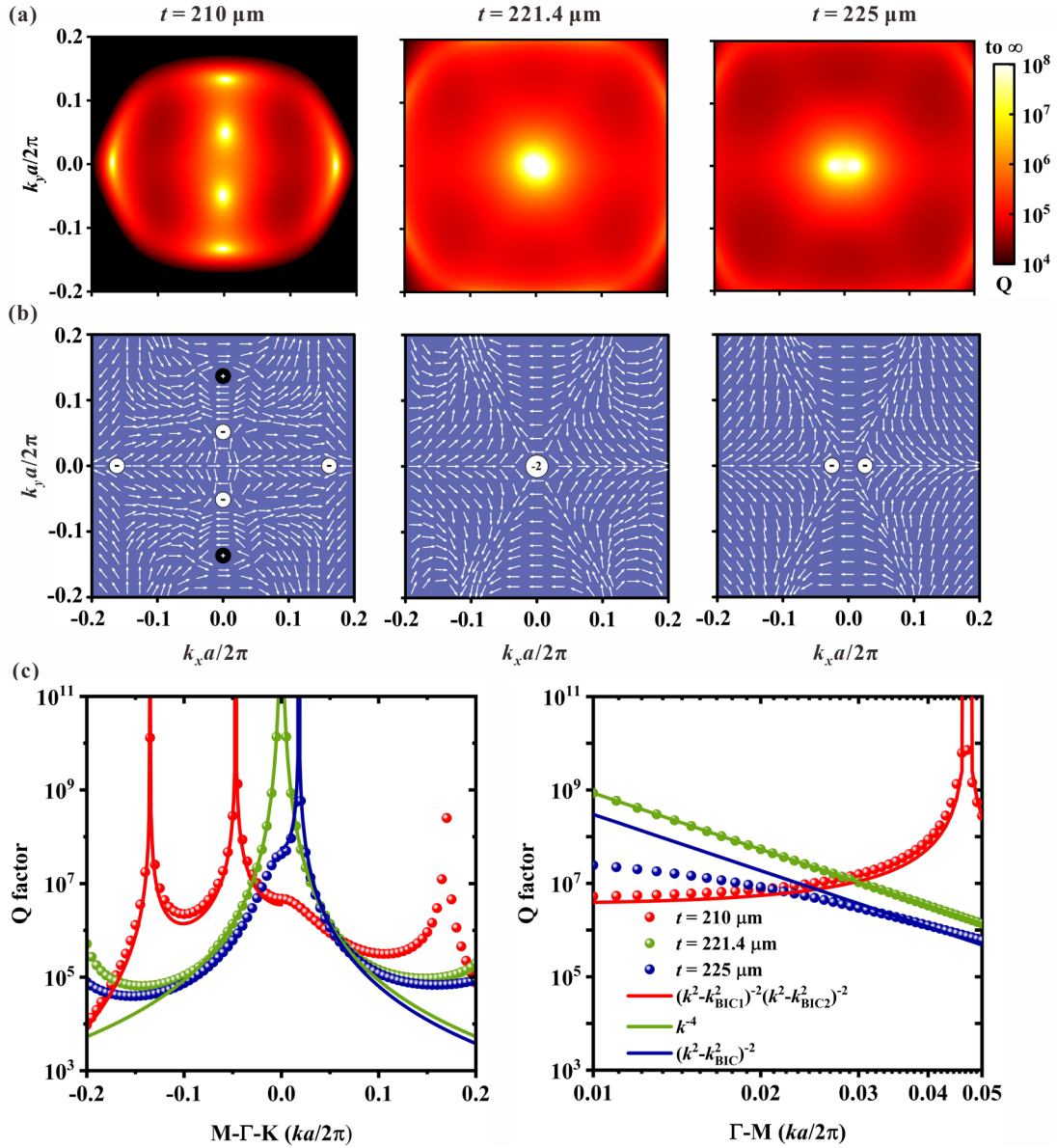
FIG. 5. Numerically calculated radiative Q factors (a) and far-field polarization state distribution (b) around BIC in the k space at $t = 210\,\mu m$ (before-merging), $t = 221.4\,\mu m$ (at merging), and $t = 225\,\mu m$ (after merging). As the slab thickness t increases, two S-BIC with topological charge -1 first approach each other along the Γ-M direction, then merge at the origin for $t = 221.4\,\mu m$, and finally bouncing off each other along the Γ-K direction. (c) Calculated Q-k relationship (dotted lines) and the corresponding fitting curves (solid lines) for three different THz-MS thicknesses. Compared to the original isolated BIC, M-BIC shows an ultrahigh Q-factor distribution over a broad wave-vector range.

symmetry, as shown in Fig. 4(b). When r_1 is deviated from r_2, the symmetry of the eigenmode at the Γ point on the TE_1 band is reduced from the C_{6v} to C_{2v} point group and thus no longer supports SP-BIC [26,31]. Owing to the topological charge conservation, the original higher-order SP-BIC cannot suddenly disappear and splits into two off-Γ BIC with same charge $q = -1$, as shown in Fig. 4(c). We calculate the Q-factor distribution in the momentum space for the THz-MS with triangular lattice of elliptic air holes, as shown in Fig. 5(a), left panel. We can observe two divergent Q states at $k_{BIC2} = \pm 0.094\pi/a$ in the Γ-M direction because the system still preserves σ_x mirror symmetry. The polarization vector, as illustrated in Fig. 5(b), left panel, characterizes these two

high-Q states as carrying charges $q = -1$, as can be verified from the single degeneracy of the nodal lines of $c_x = 0$ and $c_y = 0$ (see Fig. S4, left panel, of the Supplemental Material [38]). Moreover, this reduction in symmetry also renders eight A-BIC to annihilate each other. Thus only a pair of A-BIC with charge $q = +1$ located in σ_x mirror symmetry and a pair of A-BIC with charges $q = -1$ located in σ_y mirror symmetry are preserved.

Since the THz-MS of elliptic cylindrical holes preserves inversion symmetry, two split BIC (S-BIC) derived from the original higher-order SP-BIC are inversely symmetric with respect to the center of the Brillouin region. Therefore by tuning the structural parameters of the THz-MS, these two
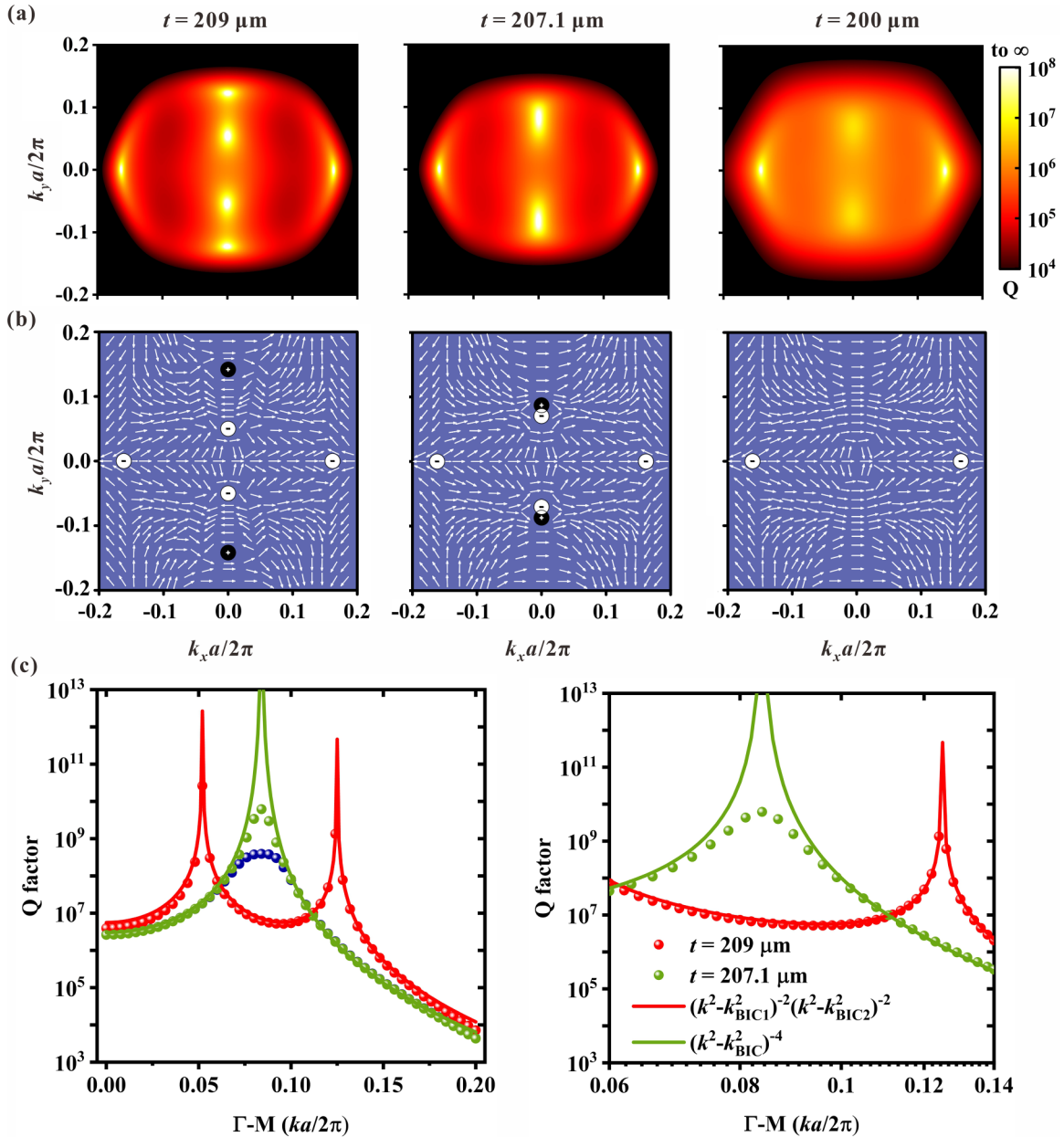
FIG. 6. Numerically calculated radiative Q factors (a) and far-field polarization state distribution (b) around BIC in the k space at $t = 209\,\mu m$ (before merging), $t = 207.1\,\mu m$ (at merging), and $t = 200\,\mu m$ (after merging). When the slab thickness t is tuned from 209 to 207.1 μm, two S-BIC with topological charge -1 merge with two A-BIC with topological charge $+1$. Further increasing t, A-BIC and the S-BIC with opposite topological charges annihilate each other and then transform into quasi-BIC modes with high Q factor. (c) Calculated radiative Q factors (dotted lines) and the corresponding fitting curves (solid lines) for three different THz-MS thicknesses. Unlike the isolated BIC case, the M-BIC case shows considerable enhancement of the Q factor for nearby states over a broad wave vector.

S-BIC will simultaneously return to the Γ point along the Γ-M direction to form a M-BIC with charge $q = -2$. We plot the evolution trajectory of BIC states in the momentum space with slab thickness t to visualize the merging phenomenon of BIC, as shown in Fig. 4(d). As the THz-MS thickness is increased from 210 to 221.4 μm, these two S-BIC move towards the center of the momentum space along the k_y axis and meet at the Γ point, as shown in Fig. 5, middle panel, and Fig. S4, middle panel, in the Supplemental Material [38]. The merging of two S-BIC at the Γ point makes it possible to excite higher-order topological charge in the structures with a

C_{2v} point group. When the slab thickness is further increased, M-BIC splits into two isolated BIC with charge $q = -1$ and then is deflected on the k_x axis, i.e., the Γ-K direction, as shown in Fig. 5, right panel, and Fig. S4, right panel, in the Supplemental Material [38]. This rejection phenomenon is inevitable because of the topological charge conservation: annihilation cannot occur between two BIC with the same topological charge. The Q factors of these two S-BIC decays as $Q \propto 1/(k^2 - k_{BIC2}^2)^2$ with respect to the distance k, while the scaling property changes to $Q \propto 1/k^4$ in the configuration in which two S-BIC merge, as shown in Fig. 5(c). A
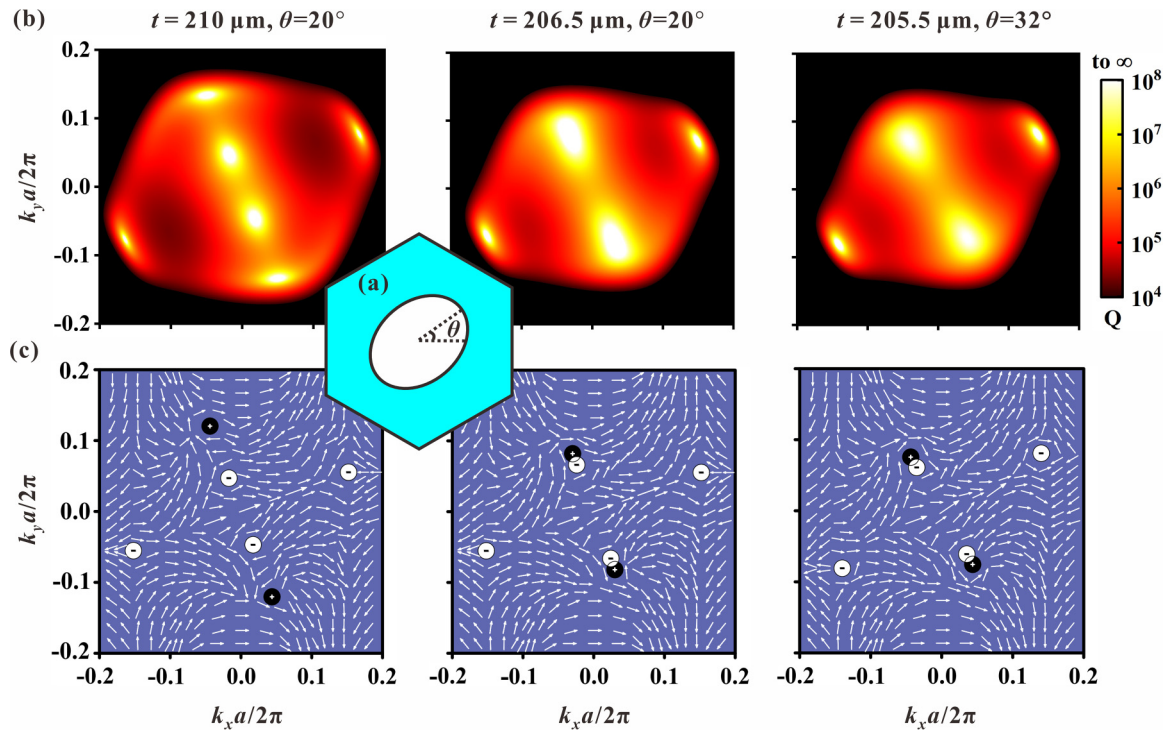
FIG. 7. (a) Schematic drawing of a triangular-lattice THz-MS of elliptic-shaped air holes with the major axis rotated by θ. Numerically calculated normalized radiative lifetime Q (b) and far-field polarization states distribution (c) around BIC in the k space for isolated BIC with $t = 210\,\mu m$ and $\theta = 20°$, M-BIC at $(k_x = \pm 0.068\pi/a, k_y = \pm 0.164\pi/a)$ with $t = 206.5\,\mu m$ and $\theta = 20°$, and M-BIC $(k_x = \pm 0.085\pi/a, k_y = \pm 0.144\pi/a)$ with $t = 205.5\,\mu m$ and $\theta = 32°$.

comparison between these two scenarios demonstrates that the Q factor of M-BIC constructed from two S-BIC are always orders of magnitude higher than those of the other two isolated S-BIC design.

In the 2D brightness map of the evolution trajectory of BIC states in Fig. 4(d), we find that when the slab thickness t decreases from $210\,\mu m$, the S-BIC gradually moves away from the Γ point along the Γ-M direction, while the two A-BIC gradually approach the Γ point along the M-Γ and K-Γ directions, respectively. The calculated Q factor [Fig. 6(a), left panel], polarization vector [Fig. 6(b), left panel], and nodal lines of c_x and c_y (see Fig. S5, left panel, of the Supplemental Material [38]) for $t = 209\,\mu m$ show that the topological charge $q = +1$ for the A-BIC and topological charge $q = -1$ for the S-BIC are all located in the Γ-M direction. As the thickness t is tuned to $207.1\,\mu m$, S-BIC meets A-BIC in the Γ-M direction, and merging happens at $k = \pm 0.168\pi/a$, as illustrated in Figs. 6(a) and 6(b), middle panel, and Fig. S5, middle panel, in the Supplemental Material [38]. By further reducing the slab thickness t, the two BIC with opposite topological charges transform into quasi-BIC states with pretty high but not divergent Q factors that subsequently and eventually annihilate each other; hence only two A-BIC with charge $q = -1$ persist in the Γ-K direction, as shown in Figs. 6(a) and 6(b), right panel, and Fig. S5, right panel, of the Supplemental Material [38]. Figure 6(c) shows the Q-factor distribution along the high-symmetry Γ-M direction for various different slab thicknesses t. When the A-BIC and S-BIC coexist at $t = 209\,\mu m$, the Q factor geometrically decays as $Q \propto 1/(k^2 - k_{BIC1}^2)^2(k^2 - k_{BIC2}^2)^2$ away from the Γ point,

where k_{BIC1} and k_{BIC2} represent a wave vector of A-BIC and S-BIC in the ΓM direction, respectively. However, when these two isolated BIC merge at $t = 207.1\,\mu m$, the scaling rule of the Q value is modified to $Q \propto 1/(k^2 - k_{BIC}^2)^4$. Compared with the isolated A-BIC or the S-BIC configuration, the M-BIC design enhances the Q factor of nearby resonances over a broad wave-vector range in the same band around the Q diverging point, which is highly desirable for photonic applications that are facilitated by strong light-matter interactions and momentum selection.

C. Merging BIC at the arbitrary points in momentum space

In-plane mirror symmetry restricts migration of BIC only to be along the highly symmetric directions. BIC are topologically stable as long as the Hermitian system maintains both $C_2^z T$ and σ_z symmetry (up-down mirror symmetry in the z direction), where C_2^z denotes a $180°$ rotation operator around the z axis, and T indicates the time-reversal operator [26,29]. Therefore, in principle, by properly tuning the structural parameters while breaking the system symmetry, the M-BIC can be achieved at arbitrary desired wave vectors. We break the all-in-plane mirror symmetries while only preserving $C_2^z T$ and σ_z symmetry by counterclockwise rotation of the elliptic air hole around the z axis with an angle θ, as illustrated in Fig. 7(a). The numerically calculated TE-like band structure of the THz-MS with thickness $t = 210\,\mu m$ and rotation angle $\theta = 20°$ are similar to that of the THz-MS of elliptic cylindrical holes (see Fig. S6 of the Supplemental Material [38]). The 2D Q map of normalized radiative

lifetime [Fig. 7(a), left panel], the polarization vector field plot [Fig. 7(b), left panel], and the single degeneracy of both nodal lines of $c_x = 0$ and $c_y = 0$ (see Fig. S7, left panel, of the Supplemental Material [38]) all explicitly indicate that isolated BIC are tuned to be away from the Γ-M direction with a specific angle. By varying the slab thickness t while keeping the other structural parameters constant, the A-BIC are forced to gradually approach the center of the k space, while the S-BIC are tuned to gradually move away from the Γ point. As a result, A-BIC and S-BIC meet in off-high-symmetric direction in the momentum space. As shown in Fig. 7, middle panel, and Fig. S7, middle panel, in the Supplemental Material [38], when the slab thickness t is tuned to 206.5 μm, these two isolated BIC merge at the point ($k_x = \pm 0.068\pi/a$, $k_y = \pm 0.164\pi/a$). The M-BIC can be excited at almost an arbitrary position in the reciprocal space as long as we select the appropriate the thickness t and rotation angle θ simultaneously. For example, the resulting M-BIC are tuned to appear at another wave vector ($k_x = \pm 0.085\pi/a$, $k_y = \pm 0.144\pi/a$) in Fig. 7, right panel (also see Fig. S7, right panel, of the Supplemental Material [38]), with $t = 205.5$ μm and $\theta = 32°$, while the other geometric parameters of the THz-MS remain unchanged.

III. CONCLUSION

In summary, we have theoretically proposed and numerically demonstrated that M-BIC can be shifted at almost arbitrary k points in the momentum space with a symmetry-broken all-Si THz-MS. The C_{6v} point group of the THz-MS ensures that the system supports the excitation of the higher-order SP-BIC as well as fundamental BIC on the lowest TE-like band. The topological nature of BIC renders the higher-order SP-BIC pinned at the high-symmetry Γ point, while A-BIC can continuously move in the k space via fine-tuning of the structural parameters. By decreasing the thickness of the THz-MS, twelve A-BIC converge to the center of the reciprocal space simultaneously and eventually merge with the SP-BIC and form a higher-order M-BIC. Furthermore, the rotational symmetry of the THz-MS is reduced to the C_{2v} point group by replacing circular air holes with elliptical cylindrical air holes. Such perturbation leads to the original higher-order SP-BIC with $q = -2$ split into two off-Γ fundamental BIC with $q = -1$ due to the topological

charge conservation. Under the increase of the THz-MS thickness, these two S-BIC approach each other and then remerge a higher-order BIC with $q = -2$ at the Γ point. In contrast, if we reduce the slab thickness, the S-BIC and A-BIC carrying opposite topological charges meet and produce M-BIC at a finite wave vector in the Γ-M direction. By rotating the elliptical cylindrical hole counterclockwise around the z axis, the all-in-plane mirror symmetries are broken while and σ_z symmetry is preserved, and the M-BIC can be realized at almost arbitrary position in the momentum space by choosing an appropriate thickness t and rotation angle θ simultaneously.

The M-BIC studied in this work can enhance the Q factor of all nearby resonances over a broad wave-vector range compared with the original isolated BIC and further improve the robustness of the BIC state against fabrication imperfections (see Figs. S8 and S9 of the Supplemental Material [38]). In addition, we have also demonstrated that all BIC states, such as at-Γ SP-BIC, off-Γ A-BIC, off-Γ S-BIC, and M-BIC, involved in this study, are topologically protected by robust polarization vortices in the momentum space. Highly confined electromagnetic fields at the M-BIC states because of the robust superhigh Q factor can substantially boost many applications requiring strong light-matter interaction, for example, ultrasensitive biochemical sensing, low-threshold quantum cascade lasers, ultra-low-power switching, and the improvement of optoelectronic device performance in the THz regime. Moreover, off-Γ M-BIC opens broad perspectives for many BIC-related applications requiring momentum selectivity, such as on-chip beam steering, directional vector beams, angle-multiplexed ultrasensitive sensors, and diffraction-free beams.

Data underlying the results presented in this paper are not publicly available at this time but may be obtained from the authors upon reasonable request

ACKNOWLEDGMENTS

The authors declare no conflicts of interest.

[1] M.-S. Hwang, H.-C. Lee, K.-H. Kim, K.-Y. Jeong, S.-H. Kwon, K. Koshelev, Y. Kivshar, and H.-G. Park, Ultralow-threshold laser using super-bound states in the continuum, Nat. Commun. **12**, 4135 (2021).

[2] Y. Yu, A. Sakanas, A. R. Zali, E. Semenova, K. Yvind, and J. Mørk, Ultra-coherent fano laser based on a bound state in the continuum, Nat. Photon. **15**, 758 (2021).

[3] S. Xiao, M. Qin, J. Duan, F. Wu, and T. Liu, Polarization-controlled dynamically switchable high-harmonic generation from all-dielectric metasurfaces governed by dual bound states in the continuum, Phys. Rev. B **105**, 195440 (2022).

[4] F. Ye, Y. Yu, X. Xi, and X. Sun, Second-harmonic generation in etchless lithium niobate nanophotonic waveguides with bound states in the continuum, Laser Photonics Rev. **16**, 2100429 (2022).

[5] X. Li, J. Ma, S. Liu, P. Huang, B. Chen, D. Wei, and J. Liu, Efficient second harmonic generation by harnessing bound states in the continuum in semi-nonlinear etchless lithium niobate waveguides, Light Sci. Appl. **11**, 317 (2022).

[6] Y. Wang, B.-Y. Xie, Y.-H. Lu, Y.-J. Chang, H.-F. Wang, J. Gao, Z.-Q. Jiao, Z. Feng, X.-Y. Xu, F. Mei *et al.*, Quantum superposition demonstrated higher-order topological bound states in the continuum, Light Sci. Appl. **10**, 173 (2021).

[7] K. Koshelev, S. Kruk, E. Melik-Gaykazyan, J.-H. Choi, A. Bogdanov, H.-G. Park, and Y. Kivshar, Subwavelength dielectric resonators for nonlinear nanophotonics, Science **367**, 288 (2020).

[8] M. Minkov, D. Gerace, and S. Fan, Doubly resonant $\chi^{(2)}$ nonlinear photonic crystal cavity based on a bound state in the continuum, Optica **6**, 1039 (2019).

[9] Z. Liu, Y. Xu, Y. Lin, J. Xiang, T. Feng, Q. Cao, J. Li, S. Lan, and J. Liu, High-Q quasibound states in the continuum for nonlinear metasurfaces, Phys. Rev. Lett. **123**, 253901 (2019).

[10] C. W. Hsu, B. Zhen, J. Lee, S.-L. Chua, S. G. Johnson, J. D. Joannopoulos, and M. Soljačić, Observation of trapped light within the radiation continuum, Nature (London) **499**, 188 (2013).

[11] W. Wang, Y. K. Srivastava, T. C. Tan, Z. Wang, and R. Singh, Brillouin zone folding driven bound states in the continuum, Nat. Commun. **14**, 2811 (2023).

[12] L. Huang, R. Jin, C. Zhou, G. Li, L. Xu, A. Overvig, F. Deng, X. Chen, W. Lu, A. Alù *et al.*, Ultrahigh-Q guided mode resonances in an all-dielectric metasurface, Nat. Commun. **14**, 3433 (2023).

[13] J. Tian, Q. Li, P. A. Belov, R. K. Sinha, W. Qian, and M. Qiu, High-Q all-dielectric metasurface: Super and suppressed optical absorption, ACS Photonics **7**, 1436 (2020).

[14] C. W. Hsu, B. Zhen, A. D. Stone, J. D. Joannopoulos, and M. Soljačić, Bound states in the continuum, Nat. Rev. Mater. **1**, 16048 (2016).

[15] L. Huang, L. Xu, D. A. Powell, W. J. Padilla, and A. E. Miroshnichenko, Resonant leaky modes in all-dielectric metasystems: Fundamentals and applications, Phys. Rep. **1008**, 1 (2023).

[16] S. Li, B. Ma, Q. Li, and M. V. Rybin, Antenna-based approach to fine control of supercavity mode quality factor in metasurfaces, Nano Lett. **23**, 6399 (2023).

[17] S. Han, L. Cong, Y. K. Srivastava, B. Qiang, M. V. Rybin, A. Kumar, R. Jain, W. X. Lim, V. G. Achanta, S. S. Prabhu *et al.*, All-dielectric active terahertz photonics driven by bound states in the continuum, Adv. Mater. **31**, 1901921 (2019).

[18] G. Zito, G. Sanità, B. Guilcapi Alulema, S. N. Lara Yépez, V. Lanzio, F. Riminucci, S. Cabrini, M. Moccia, C. Avitabile, A. Lamberti *et al.*, Label-free DNA biosensing by topological light confinement, Nanophotonics **10**, 4279 (2021).

[19] Y. Jahani, E. R. Arvelo, F. Yesilkoy, K. Koshelev, C. Cianciaruso, M. De Palma, Y. Kivshar, and H. Altug, Imaging-based spectrometer-less optofluidic biosensors based on dielectric metasurfaces for detecting extracellular vesicles, Nat. Commun. **12**, 3246 (2021).

[20] Y. Ren, P. Li, Z. Liu, Z. Chen, Y.-L. Chen, C. Peng, and J. Liu, Low-threshold nanolasers based on miniaturized bound states in the continuum, Sci. Adv. **8**, eade8817 (2022).

[21] A. Kodigala, T. Lepetit, Q. Gu, B. Bahari, Y. Fainman, and B. Kanté, Lasing action from photonic bound states in continuum, Nature (London) **541**, 196 (2017).

[22] B. Wang, W. Liu, M. Zhao, J. Wang, Y. Zhang, A. Chen, F. Guan, X. Liu, L. Shi, and J. Zi, Generating optical vortex beams by momentum-space polarization vortices centred at bound states in the continuum, Nat. Photon. **14**, 623 (2020).

[23] L. Kang, Y. Wu, X. Ma, S. Lan, and D. H. Werner, High-harmonic optical vortex generation from photonic bound states in the continuum, Adv. Opt. Mater. **10**, 2101497 (2022).

[24] G. Zograf, K. Koshelev, A. Zalogina, V. Korolev, R. Hollinger, D.-Y. Choi, M. Zuerch, C. Spielmann, B. Luther-Davies, D. Kartashov *et al.*, High-harmonic generation from resonant dielectric metasurfaces empowered by bound states in the continuum, ACS Photonics **9**, 567 (2022).

[25] Q. Liu, L. Qu, Z. Gu, D. Zhang, W. Wu, W. Cai, M. Ren, and J. Xu, Boosting second harmonic generation by merging bound states in the continuum, Phys. Rev. B **107**, 245408 (2023).

[26] B. Zhen, C. W. Hsu, L. Lu, A. D. Stone, and M. Soljačić, Topological nature of optical bound states in the continuum, Phys. Rev. Lett. **113**, 257401 (2014).

[27] Y. Zhang, A. Chen, W. Liu, C. W. Hsu, B. Wang, F. Guan, X. Liu, L. Shi, L. Lu, and J. Zi, Observation of polarization vortices in momentum space, Phys. Rev. Lett. **120**, 186103 (2018).

[28] J. Jin, X. Yin, L. Ni, M. Soljačić, B. Zhen, and C. Peng, Topologically enabled ultrahigh-Q guided resonances robust to out-of-plane scattering, Nature (London) **574**, 501 (2019).

[29] M. Kang, S. Zhang, M. Xiao, and H. Xu, Merging bound states in the continuum at off-high symmetry points, Phys. Rev. Lett. **126**, 117402 (2021).

[30] M. Kang, L. Mao, S. Zhang, M. Xiao, H. Xu, and C. T. Chan, Merging bound states in the continuum by harnessing higher-order topological charges, Light Sci. Appl. **11**, 228 (2022).

[31] T. Yoda and M. Notomi, Generation and annihilation of topologically protected bound states in the continuum and circularly polarized states by symmetry breaking, Phys. Rev. Lett. **125**, 053902 (2020).

[32] Y. Kurosaka, S. Iwahashi, Y. Liang, K. Sakai, E. Miyai, W. Kunishi, D. Ohnishi, and S. Noda, On-chip beam-steering photonic-crystal lasers, Nat. Photon. **4**, 447 (2010).

[33] S. T. Ha, Y. H. Fu, N. K. Emani, Z. Pan, R. M. Bakker, R. Paniagua-Domínguez, and A. I. Kuznetsov, Directional lasing in resonant semiconductor nanoantenna arrays, Nat. Nanotechnol. **13**, 1042 (2018).

[34] S. I. Azzam, K. Chaudhuri, A. Lagutchev, Z. Jacob, Y. L. Kim, V. M. Shalaev, A. Boltasseva, and A. V. Kildishev, Single and multi-mode directional lasing from arrays of dielectric nanoresonators, Laser Photonics Rev. **15**, 2000411 (2021).

[35] F. Yesilkoy, E. R. Arvelo, Y. Jahani, M. Liu, A. Tittl, V. Cevher, Y. Kivshar, and H. Altug, Ultrasensitive hyperspectral imaging and biodetection enabled by dielectric metasurfaces, Nat. Photon. **13**, 390 (2019).

[36] A. Tittl, A. Leitis, M. Liu, F. Yesilkoy, D.-Y. Choi, D. N. Neshev, Y. S. Kivshar, and H. Altug, Imaging-based molecular barcoding with pixelated dielectric metasurfaces, Science **360**, 1105 (2018).

[37] Y. Lin, T. Feng, S. Lan, J. Liu, and Y. Xu, On-chip diffraction-free beam guiding beyond the light cone, Phys. Rev. Appl. **13**, 064032 (2020).

[38] See Supplemental Material at http://link.aps.org/supplemental/10.1103/PhysRevB.109.035406 for details and discussion of theoretical models for scaling rules of the Q factor, electromagnetic multipole decomposition, distributions of Stokes parameter S_3 in the momentum space, evolution of the band

structures of the lowest frequency TE-like eigenmode with the variation of structure symmetry, the distributions of absolute value of the nodal line c_x and c_y in the k space, and the robustness of the Q factor of M-BIC against fabrication imperfection,

[39] Y. Zeng, G. Hu, K. Liu, Z. Tang, and C.-W. Qiu, Dynamics of topological polarization singularity in momentum space, Phys. Rev. Lett. **127**, 176101 (2021).

[40] W. Ye, Y. Gao, and J. Liu, Singular points of polarizations in the momentum space of photonic crystal slabs, Phys. Rev. Lett. **124**, 153904 (2020).

[41] W. Liu, B. Wang, Y. Zhang, J. Wang, M. Zhao, F. Guan, X. Liu, L. Shi, and J. Zi, Circularly polarized states spawning from bound states in the continuum, Phys. Rev. Lett. **123**, 116104 (2019).